






## Higher-dimensional spin selectivity in chiral crystals

Yinong Zhou <sup>1</sup>, Dmitri Leo M. Cordova <sup>2</sup>, Griffin M. Milligan <sup>2</sup>, Maxx Q. Arguilla <sup>2</sup> and Ruqian Wu <sup>1,\*</sup>

<sup>1</sup>*Department of Physics and Astronomy, University of California, Irvine, California 92697-4575, USA*

<sup>2</sup>*Department of Chemistry, University of California, Irvine, California 92697-4575, USA*



(Received 3 May 2023; revised 6 July 2024; accepted 9 July 2024; published 22 July 2024)

This study aims to investigate the interplay between chiral-induced spin-orbit coupling along the screw axis and antisymmetric spin-orbit coupling (ASOC) in the normal plane within a chiral crystal, using both general model analysis and first-principles simulations of InSeI, a chiral van der Waals crystal. While chiral molecules of light atoms typically exhibit spin selectivity only along the screw axis, chiral crystals with heavier atoms can have strong ASOC effects that influence spin-momentum locking in all directions. The resulting phase diagram of spin accumulation shows the potential for controlling phase transition and flipping spin by reducing symmetry through surface cleavage, thickness reduction or strain. We also experimentally synthesized high-quality InSeI crystals to demonstrate the feasibility and thermal stability of the proposed material. This lays a solid foundation for the realization of transverse spin selectivity in chiral crystals, facilitating the development of spintronic devices.

DOI: [10.1103/PhysRevB.110.045434](https://doi.org/10.1103/PhysRevB.110.045434)

### I. INTRODUCTION

Chiral structures, geometrically unable to be superimposed on their mirror images, are found abundantly in nature [1–3], from molecules to larger-scale chiral crystals [4] and metamaterials [5–7]. The presence of chirality can dictate a substance’s optical, magnetic, and electronic properties, such as magnetochiral dichroism [8,9], magnetic skyrmion [10,11], and electrical magnetochiral anisotropy [12–14], promising diverse applications. One important phenomenon in this context is the chiral-induced spin selectivity (CISS) [15–19]. As electrons traverse a chiral system, those with a specific spin orientation are transmitted more preferentially than the opposite spin. The ability to harness electron spin has the potential to expedite data transfer, reduce power usage, and augment memory and processing capabilities [20–22] for the use in spintronics and quantum technologies [23].

Spin-orbit coupling (SOC) plays a crucial role in the CISS effect [16–18]. Studies on chiral molecules, such as the archetypal double helix DNA [24–26], have demonstrated that the inherent chiral potential induces a substantial SOC, which yields significant spin polarization along the screw axis [27–29]. For an electron moving in a single helix chain with a momentum  $\mathbf{p}$ , the SOC can be expressed as  $H_{\text{SOC}} = \frac{\hbar}{4m^2c^2} \nabla V \cdot (\boldsymbol{\sigma} \times \mathbf{p})$ , where  $\hbar$  is the reduced Planck’s constant,  $m$  is the electron mass,  $c$  is the speed of light,  $V$  is the electrostatic potential, and  $\boldsymbol{\sigma} = (\sigma_x, \sigma_y, \sigma_z)$  represents the Pauli matrices. In one-dimensional (1D) chains, the terms containing  $\sigma_x$  and  $\sigma_y$  are canceled by oscillation, leaving only the  $\sigma_z$  term to contribute to the spin polarization along the screw axis. This results in a chiral-induced SOC (CISOC)  $H_c = \lambda_C k_z \sigma_z$ , where  $\lambda_C$  is the strength of CISOC [30].

Chiral crystals have three-dimensional (3D) periodicity, and thus introduce additional complexities and opportunities

to study new chirality-induced phenomena. First, one may anticipate the development of spin current in all three dimensions, offering greater flexibility for device design. Furthermore, compared to chiral molecules, the SOC effect in chiral crystals can be considerably stronger and adjustable by manipulating symmetry and incorporating heavy atoms. Research in chiral crystals has been previously limited to Kramers-Weyl fermions in metallic states or minimal bandgaps [31–34]. Studies of spin selectivity in chiral crystals may open new avenues for developing new materials and technologies.

There is growing interest in crystals with 1D subunits that are held together by weak interactions such as van der Waals (vdW) or ionic bonding [35–38]. Many of them exhibit structural chirality within each 1D unit, for example, tellurium nanowires [39,40], tantalum disilicide [41], and monoaxial chiral dichalcogenide [42,43]. Typically, the CISOC strength in these materials is substantially larger than the antisymmetric SOC (ASOC) strength, leading to the omission of the ASOC effect normal to the screw axis in previous studies [44]. However, the ASOC becomes particularly important for some crystals, such as indium seleniodide (InSeI), which consists of a bundle of atomically precise 1D helical chains with heavy elements and a huge twist angle ( $135^\circ$ ) [45,46,47]. The significant ASOC, in tandem with CISOC, may give rise to unique spin configurations in the 3D Brillouin zone.

In this article, we investigate the interplay of CISOC and ASOC and establish a phase diagram of the spin accumulation with varying four ASOC contributions. When Weyl or Dresselhaus SOC dominates in a chiral crystal, it leads to a high-spin-accumulation phase which has spin selectivity in three directions. This interesting finding is verified by first-principles calculations on a chiral helical vdW crystal, indium seleniodide (InSeI), whose valence band exhibits higher-dimensional spin selectivity with the dominating Weyl ASOC coupled with CISOC. Furthermore, we find that a phase

\*Contact author: wur@uci.edu

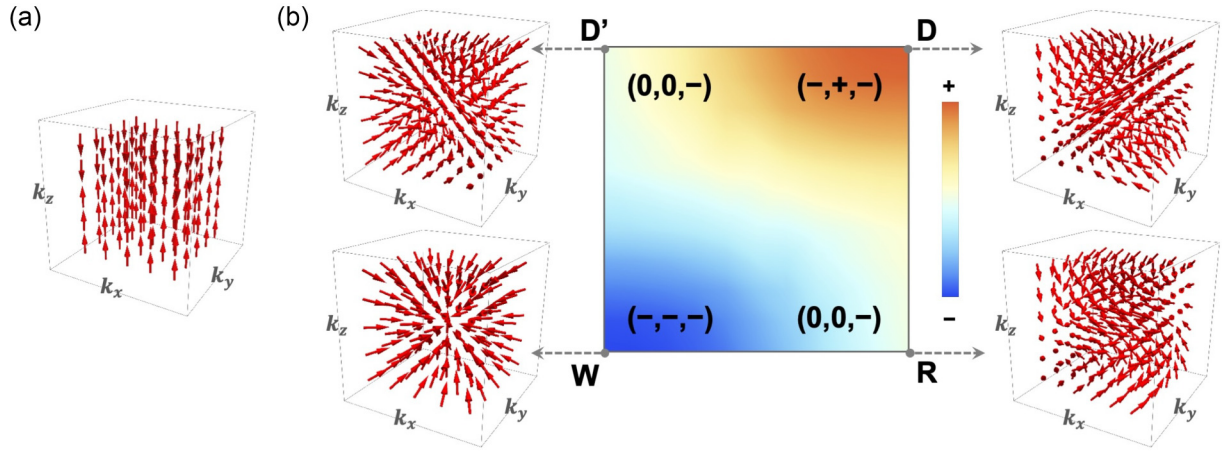


FIG. 1. (a) 3D spin texture of the CISOC. (b) Phase diagram of spin accumulation  $A^\nu$  with the interplay of CISOC with different ASOC contributions including the Rashba (R), Weyl (W), and two types of Dresselhaus (D and D') SOCs. The phases of  $(-, -, -)$ ,  $(-, +, -)$ , and  $(0, 0, -)$  represent the sign of spin accumulation in  $x, y, z$  directions, where  $+$  and  $-$  represent the spin is parallel or antiparallel with the current direction, and  $0$  represents  $+$  and  $-$  spins are canceled out. The color represents the strength of the spin accumulation.

transition with spin-flipping can be induced by symmetry reduction. As a major step toward the realization, we experimentally show that a chiral (110) surface can be exposed in the thermodynamically stable achiral analog of InSeI. It is worth noting that the unique spin configurations of InSeI can potentially be extended to other quasi-1D crystals within the  $MX_Y$  family ( $M = \text{Ga, In}$ ;  $X = \text{Se, Te}$ ;  $Y = \text{Cl, Br, I}$ ) [48].

## II. SOC HAMILTONIAN AND MODEL ANALYSIS

To give a general picture of the interplay of ASOC and CISOC, we write the SOC Hamiltonian using a  $\mathbf{k} \cdot \mathbf{p}$  model with a chiral crystal with the screw axis along the  $z$  direction:

$$\begin{aligned} H_{\text{SOC}} &= H_R + H_W + H_D + H_{D'} + H_C \\ &= \lambda_R(\sigma_x k_y - \sigma_y k_x) + \lambda_W(\sigma_x k_x + \sigma_y k_y) \\ &\quad + \lambda_D(\sigma_x k_x - \sigma_y k_y) + \lambda_{D'}(\sigma_x k_y + \sigma_y k_x) + \lambda_C k_z \sigma_z, \end{aligned} \quad (1)$$

where  $\lambda_i$  ( $i = R, W, D, D', C$ ) represents the strength of each SOC term. The first four terms are ASOCs including Rashba SOC ( $H_R$ ) with tangential spin texture  $\vec{S} = (k_y, -k_x, 0)$ ; Weyl SOC ( $H_W$ ) with radial spin texture  $\vec{S} = (k_x, k_y, 0)$ ; and two Dresselhaus SOCs ( $H_D$  and  $H_{D'}$ ) with tangential-radial spin textures  $\vec{S} = (k_x, -k_y, 0)$  and  $\vec{S} = (k_y, k_x, 0)$ , respectively. The last term is the CISOC ( $H_C$ ), where the spin texture can be expressed as  $\vec{S} = (0, 0, k_z)$ . Solving the Hamiltonian in Eq. (1), we can get analytical solutions of spin texture for the spin-up state as  $\vec{S} = (S^x, S^y, S^z)$ , where

$$\begin{aligned} S^x &= \mp \frac{2}{N^2} \frac{(\lambda_W + \lambda_D)k_x + (\lambda_R + \lambda_{D'})k_y}{\lambda_C k_z \pm \varepsilon}, \\ S^y &= \mp \frac{2}{N^2} \frac{(\lambda_{D'} - \lambda_R)k_x + (\lambda_W - \lambda_D)k_y}{\lambda_C k_z \pm \varepsilon}, \\ S^z &= \mp \frac{2}{N^2} \frac{\lambda_C k_z}{\lambda_C k_z \pm \varepsilon}, \end{aligned} \quad (2)$$

for  $k_z \geq 0$  and  $k_z < 0$ , respectively.  $\varepsilon$  represents the absolute value of the eigenvalues of  $H_{\text{SOC}}$ . The 3D spin texture is

plotted in Fig. 1. With only CISOC, the spin orientation always points to the  $-\hat{k}_z$  direction, as shown in Fig. 1(a). However, additional ASOC terms lead to much richer spin textures, as shown in Fig. 1(b). More detailed derivations are shown in Sec. I of the Supplemental Material [54].

Next, we discuss spin selectivity induced by the interplay of ASOC and CISOC. When a charge current flows in one direction, it induces a shift in the Fermi surface in the negative direction, resulting in an imbalance of spin accumulation. This mechanism of charge-to-spin conversion, known as the Edelstein effect, is widely recognized in phenomena such as the spin Hall effect (SHE) [49] and the Rashba-Edelstein effect [50–52]. With only CISOC, the spin selectivity only occurs in the  $k_z$  direction. However, with additional ASOC terms, the spin selectivity can be realized in all three dimensions. To visualize this behavior, we construct a phase diagram of spin accumulation in Fig. 1(b) with the different contributions of ASOCs cooperating with a consistent CISOC strength.

The spin accumulation is calculated using the semiclassical Boltzmann transport theory [53]. With a charge current along the  $\nu = x, y, z$  direction, the charge current density  $\vec{j}_c$  is given by [51]

$$\vec{j}_c^\nu = |e|^2 \sum_{\vec{k}} (\vec{\Lambda}_{\vec{k}}^\nu \cdot \vec{E}) \delta(\mathcal{E}_{\vec{k}}^\nu - \mathcal{E}_F) \vec{v}_{\vec{k}}^\nu. \quad (3)$$

The current-induced spin density is given by

$$\vec{S}^\nu = -|e| \sum_{\vec{k}} (\vec{\Lambda}_{\vec{k}}^\nu \cdot \vec{E}) \delta(\mathcal{E}_{\vec{k}}^\nu - \mathcal{E}_F) \vec{S}_{\vec{k}}^\nu. \quad (4)$$

The mean free path in the relaxation-time approximation is  $\Lambda_{\vec{k}}^\nu = \tau_{\vec{k}}^\nu \vec{v}_{\vec{k}}^\nu$ , where  $\tau_{\vec{k}}^\nu$  is the transport lifetime, the group velocity is  $\vec{v}_{\vec{k}}^\nu = \frac{1}{\hbar} \nabla_{\vec{k}} \mathcal{E}_{\vec{k}}^\nu$ , and  $\vec{E}$  is an external electric field. The spin accumulation can then be calculated as  $A^\nu = \vec{S}^\nu / \vec{j}_c^\nu$ .

In Fig. 1(b), with only Weyl and CISOC  $\lambda_W = \lambda_C$  (other  $\lambda_i = 0$ ), the spin accumulation is negative in all three directions, leading to a  $(-, -, -)$  phase. For  $\lambda_D = \lambda_C$  (other  $\lambda_i = 0$ ), the spin accumulation is positive in the  $k_y$  direction

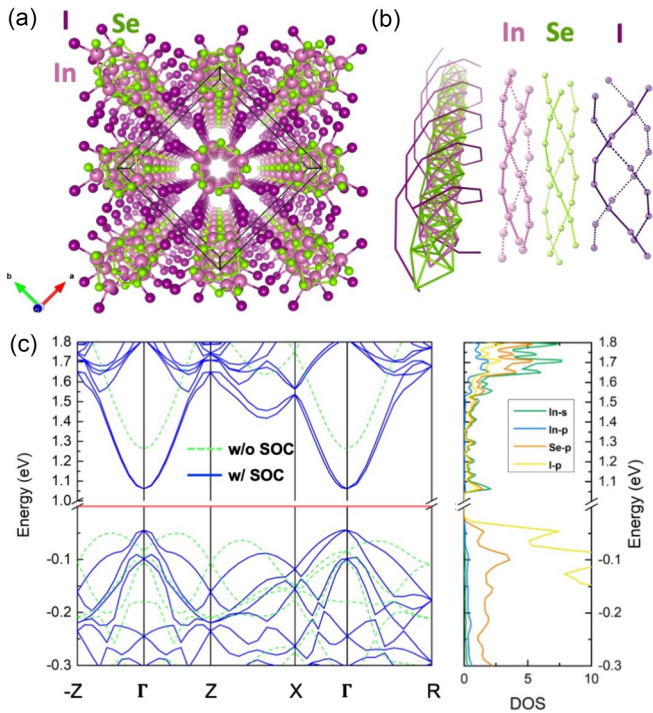


FIG. 2. Lattice and band structure of InSeI. (a) The bulk crystal with right-handed chirality. (b) The 1D nanochain with the decomposed chains for In, Se, and I, respectively. (c) The band structures of the bulk in (a) with and without SOC and the orbital projected DOS with the green, blue, orange, and yellow lines represent In- $s$ , In- $p$ , Se- $p$ , and I- $p$  orbitals, respectively.

but negative in  $k_x$  and  $k_z$  directions, resulting in a  $(-, +, -)$  phase. For  $\lambda_R = \lambda_C$  or  $\lambda_D = \lambda_C$  (other  $\lambda_i = 0$ ), the spin accumulation is canceled out due to the tangential spin texture in  $k_x$  and  $k_y$  directions; but in the  $k_z$  direction, the spin selectivity survives due to the structure chirality, resulting in a  $(0, 0, -)$  phase. More detailed discussions of the phase diagram can be found in Sec. II of the Supplemental Material [54]. As the ASOCs can be tuned by reducing symmetry through surface cleavage, thickness reduction, or strain, the possibility of having a rich spin texture and spin selectivity in a single system is very intriguing for the development of spintronic devices.

### III. FIRST-PRINCIPLES CALCULATION OF A REAL MATERIAL

For the realization of this model, one needs to find chiral crystals with large ASOCs. As shown in Figs. 2(a) and 2(b), we construct a chiral InSeI crystal formed by 1D helical chains with the  $[\text{InSe}_3]_n$  tetrahedral motif wherein each distinct elemental site following a tetrahelix is defined by a large  $135^\circ$  twist angle. These helical chains are stacked through weak vdW interactions. As shown in Fig. 2(a), the bulk InSeI with space group  $P4_3$  shows the right-handed chirality with a screw symmetry including a  $C_4$  rotational symmetry in the  $xy$  plane and a  $c/4$  translational symmetry along the  $z$  direction, where  $c$  represents the lattice constant along the  $z$  direction. Aside from the structural chirality, all elements in InSeI show

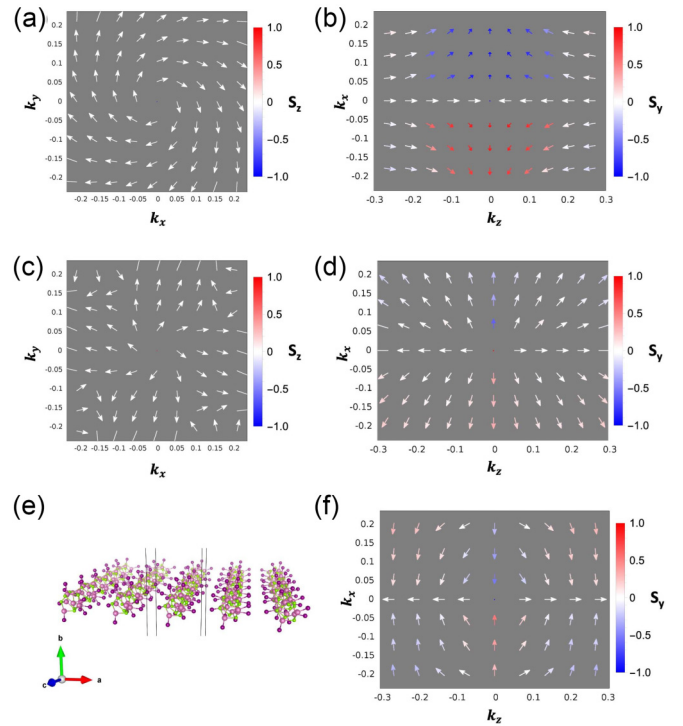


FIG. 3. The spin texture of the first (a), (b) conduction and (c), (d) valence band in the (a), (c)  $k_x$ - $k_y$  plane and (b), (d)  $k_z$ - $k_x$  plane, respectively. The color of the spin vectors represents the out-of-plane spin component. (e) The lattice structure of the monolayer for the (100) surface of the bulk in Fig. 2(a). (f) The spin texture of the first valence band of the monolayer in (e).

a strong intrinsic SOC strength, especially in the heavier I atoms [55]. With the SOC included, the electronic band structure from the density functional calculations (DFT) shows spin splitting in both directions along and normal to the screw axis, as shown in Fig. 2(c). The valence band splitting is larger than that of conduction bands because the valence bands are mainly contributed by I- $p$  orbitals with large SOC strength, as also reflected by the projected density of states (DOS) shown in Fig. 2(c). The calculation method and parameters are described in Sec. III of the Supplemental Material [54].

To investigate spin configurations, we plot the spin texture for the first conduction and valence band, as shown in Figs. 3(a)–3(d). As the bulk InSeI has the  $C_4$  rotational symmetry in the normal plane, i.e., the  $k_x$ - $k_y$  plane, only Rashba and Weyl ASOC are allowed [56]. For the first conduction band, the spin in the  $k_x$ - $k_y$  plane shows a tangential texture, corresponding to a Rashba-dominant ASOC [see Fig. 3(a)]. In contrast, the first valence band shows a radial spin texture, corresponding to a Weyl-dominant ASOC [see Fig. 3(c)]. Through the interplay with the CISOC in the  $k_z$  direction, the conduction band shows a tangential-radial spin texture in the  $k_z$ - $k_x$  plane [see Fig. 3(b)], while the valence band shows a radial spin texture [see Fig. 3(d)]. Importantly, we may extract SOC strength by fitting the spin textures obtained from the model and first-principle calculations, as  $\lambda_R/\lambda_W = -S^y/S^x$  for  $k_y = k_z = 0$ ; and  $\lambda_W/\lambda_C = S^x k_z / (S^z k_x)$  for  $k_y = 0$ . Using  $\lambda_C = C$  ( $C$  is a constant) as the unit, we get  $\lambda_W = -0.5\lambda_C$  and  $\lambda_R = -1.2\lambda_C$  for the first conduction band [Figs. 3(a)

and 3(b)]. For the first valence band [Figs. 3(c), 3(d)], we get  $\lambda_W = 1.5\lambda_C$  and  $\lambda_R = 0.7\lambda_C$ . Details of the fitting procedure and the opposite spin textures for the second conduction and valence bands are discussed in Sec. IV of the Supplemental Material [54]. Considering the spin accumulation in 3D, the conduction band corresponds to the Rashba-dominant  $(0, 0, -)$  phase in Fig. 1(b) with only one direction spin selectivity in the  $k_z$  direction. The valence band corresponds to the Weyl-dominant  $(-, -, -)$  phase with the spin selectivity in all three directions. The phase diagram for the valence band of InSeI with the opposite sign of the Dresselhaus SOC is discussed in Figs. S4–S7 in Sec. II of the Supplemental Material [54].

Because ASOC is sensitive to crystalline symmetry, we explore the possibility of introducing the Dresselhaus SOC in InSeI by reducing its symmetry to  $C_2$ . Different from  $C_4$  symmetry that only has Rashba and Weyl ASOCs, the  $C_2$  symmetry allows all four ASOCs [56]. We constructed a monolayer of nanochains in the  $(100)$  plane, as shown in Fig. 3(e). The spin texture for the first valence band becomes a tangential-radial type in the  $k_z$ - $k_x$  plane [see Fig. 3(f)]. By fitting the spin texture around the  $\Gamma$  point, we find that except Rashba and Weyl SOC, Dresselhaus SOC terms are introduced with  $\lambda_D = -2.7\lambda_C$  and  $\lambda_{D'} = 0.4\lambda_C$  [54]. The strong Dresselhaus SOC leads to a phase transition from the Weyl-dominant  $(-, -, -)$  phase to the Dresselhaus-dominant  $(+, -, -)$  phase with the opposite spin selectivity in the  $x$  direction, comparing Figs. 3(d) and 3(f). The phase transition is labeled in the spin-down phase diagram in Fig. S5 [54]. The phase transition can also be induced by applying compressive strain on the bulk to reduce the symmetry. A gradual spin-flipping of the spin texture along the  $k_x$  direction can be found in Fig. S12 in Sec. IV of the Supplemental Material [54].

#### IV. EXPERIMENTAL SYNTHESIS

Excitingly, we can synthesize sizable high-quality chiral crystals of the reported thermodynamically stable analog of InSeI [45,47]. The synthesis method can be found in Sec. V of the Supplemental Material [54]. As shown in the scanning electron microscopy (SEM) images in Figs. 4(a) and 4(b), the air- and temperature-stable sample displays a cleavable stepped surface which reflects the 1D vdW structure in the bulk. The energy-dispersive spectroscopy (EDS) shows the purity and uniform distribution of the constituent In, Se, and I elements in the structure [Fig. 4(c)]. However, it is important to note that the experimentally synthesized InSeI crystallizes in the achiral space group  $I4_1/a$  [42,44], which contains both handedness (left and right handedness) of the helices, as shown in the insert on the top right of Fig. 4(d). Encouragingly, owing to the vdW interaction between the helical chains and the intrinsic size of the crystals, InSeI crystals are readily cleavable and orientable in select facets parallel to the long chain direction, as shown in Fig. 4(b). These properties of the bulk crystals allow for the exposure of a  $(110)$  surface which corresponds to a surface comprised of helices with only one type of handedness, as the dashed line shown in the insets of Fig. 4(d). High-resolution transmission electron microscopy (HRTEM) imaging and the corresponding indexing of the fast

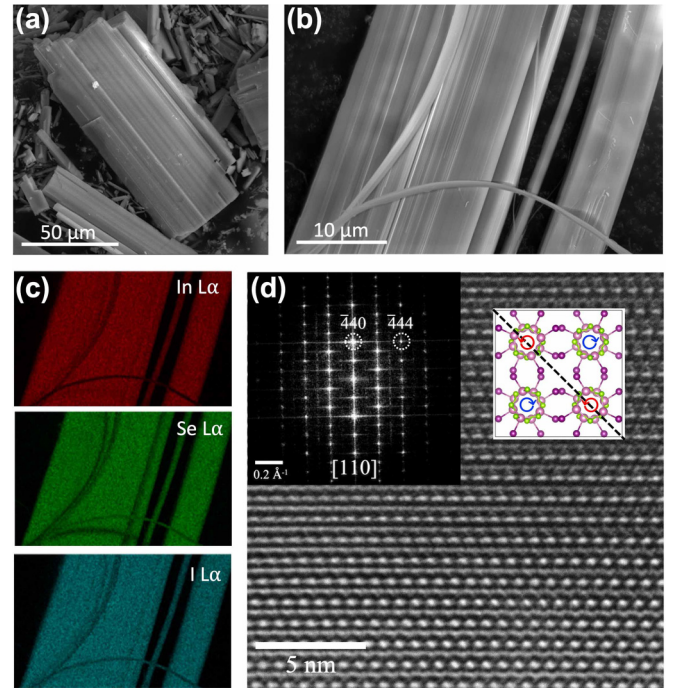


FIG. 4. (a), (b) SEM images of InSeI. (c) EDS elemental mapping of  $L\alpha$  representing the relaxation from M ( $n = 3$ ) to L ( $n = 2$ ) electrons of In, Se, and I, respectively. (d) TEM image for the  $(110)$  surface with the FFT pattern inserted on the top left. The top view of the crystal unit cell is inserted on the top right, where the black dashed line represents the  $(110)$  surface with the same chirality. The red and blue circles with arrows in the insert structure represent left- and right-handed nanochains, respectively.

Fourier transform (FFT, inset) of an exposed cleaved facet of InSeI show that it is possible to selectively cleave and expose the sought-after  $(110)$  surface of the achiral InSeI crystal, as is shown in Fig. 4(d). The corresponding calculation of the spin texture for the  $(110)$  surface can be found in Sec. IV of the Supplemental Material [37]. As expected, these calculations confirm that the  $(110)$  facet, which bears the helices with single handedness, in the monolayer regime, also involves strong Dresselhaus terms as discussed in Figs. 3(e) and 3(f). The design of a spintronic device to measure spin selectivity in three directions is discussed in Sec. VI of the Supplemental Material [54].

#### V. CONCLUSION

In conclusion, we demonstrated that the 3D spin texture arises from combining out-of-plane CISOC and in-plane ASOC, creating a phase diagram with different spin accumulation phases for 3D spin selectivity. This was verified by DFT calculations for InSeI, a chiral vdW crystal. A large spin splitting and radial spin texture were found for the first valence band, as a first example of the realization of the 3D spin selectivity in actual materials. By reducing the symmetry, a strong Dresselhaus SOC is produced, leading to a phase transition with an opposite spin selectivity along the  $k_x$  direction. As a further step, we experimentally synthesized the thermodynamically stable achiral InSeI analog and demonstrated that the  $(110)$  surface shows the aligned helices with the

same handedness. More experiments of the spin measurement using magnetic conductive probe atomic force microscopy [57] and the device applications are in progress. Our findings offer numerous advantages including greater control over the spin states, the potential for new functionalities that are not possible with monodirectional selectivity, and increased flexibility in designing and implementing spin-based technologies. We anticipate that these advancements will considerably expand the progress in the fields of quantum and spintronic materials and technologies that rely on the manipulation of spin states.

## ACKNOWLEDGMENTS

Y.Z. and R.W. were supported by DOE-BES (Grant No. DE-FG02-05ER46237). Computational simulations were performed at the U.S. Department of Energy Supercomputer Facility (NERSC). D.L.M.C., G.M.M., and M.Q.A. acknowledge the UC Irvine Materials Research Institute (IMRI) for instrumental support. Facilities and instrumentation at IMRI are supported, in part, by the National Science Foundation through the UC Irvine Materials Research Science and Engineering Center Grant No. DMR-2011967.

- 
- [1] J. Lough and I. W. Wainer, *Chirality in the Natural & Applied Sciences* (Blackwell Publishing Limited, Oxford, 2002).
- [2] G. H. Wagnière, *On Chirality and the Universal Asymmetry: Reflections on Image and Mirror Image* (Wiley-VCH, Weinheim, 2007).
- [3] N. H. Cho, A. Guerrero-Martínez, J. Ma, S. Bals, N. A. Kotov, L. M. Liz-Marzán, and K. T. Nam, *Nat. Rev. Bioeng.* **1**, 88 (2023).
- [4] H. D. Flack, *Helv. Chim. Acta* **86**, 905 (2003).
- [5] B. Wang, J. Zhou, T. Koschny, M. Kafesaki, and C. M. Soukoulis, *J. Opt. A: Pure Appl. Opt.* **11**, 114003 (2009).
- [6] Z. Wang, F. Cheng, T. Winsor, and Y. Liu, *Nanotechnology* **27**, 412001 (2016).
- [7] I. Fernandez-Corbaton, C. Rockstuhl, P. Ziemke, P. Gumbsch, A. Albiez, R. Schwaiger, T. Frenzel, M. Kadic, and M. Wegener, *Adv. Mater.* **31**, 1807742 (2019).
- [8] G. Rikken and E. Raupach, *Nature (London)* **390**, 493 (1997).
- [9] N. Berova, K. Nakanishi, and R. W. Woody, *Circular Dichroism: Principles and Applications* (Wiley, New York, NY, 2009).
- [10] A. Bogdanov and A. Hubert, *J. Magn. Magn. Mater.* **138**, 255 (1994).
- [11] N. Nagaosa and Y. Tokura, *Nat. Nanotechnol.* **8**, 899 (2013).
- [12] G. L. J. A. Rikken, J. Fölling, and P. Wyder, *Phys. Rev. Lett.* **87**, 236602 (2001).
- [13] V. Krstić, S. Roth, M. Burghard, K. Kern, and G. Rikken, *J. Chem. Phys.* **117**, 11315 (2002).
- [14] F. Pop, P. Auban-Senzier, E. Canadell, G. L. Rikken, and N. Avarvari, *Nat. Commun.* **5**, 3757 (2014).
- [15] R. Naaman and D. H. Waldeck, *J. Phys. Chem. Lett.* **3**, 2178 (2012).
- [16] R. Naaman and D. H. Waldeck, *Annu. Rev. Phys. Chem.* **66**, 263 (2015).
- [17] S. Dalum and P. Hedegård, *Nano Lett.* **19**, 5253 (2019).
- [18] R. Naaman, Y. Paltiel, and D. H. Waldeck, *Nat. Rev. Chem.* **3**, 250 (2019).
- [19] J. Fransson, *Isr. J. Chem.* **62**, e202200046 (2022).
- [20] A. Hirohata and K. Takanashi, *J. Phys. D* **47**, 193001 (2014).
- [21] S. Bandyopadhyay and M. Cahay, *Introduction to Spintronics* (CRC Press, Boca Raton, FL, 2015).
- [22] N. Nanotechnology, *Nat. Nanotechnol.* **10**, 185 (2015).
- [23] A. Hirohata, K. Yamada, Y. Nakatani, I.-L. Prejbeanu, B. Diény, P. Pirro, and B. Hillebrands, *J. Magn. Magn. Mater.* **509**, 166711 (2020).
- [24] B. Göhler, V. Hamelbeck, T. Markus, M. Kettner, G. Hanne, Z. Vager, R. Naaman, and H. Zacharias, *Science* **331**, 894 (2011).
- [25] G.-F. Du, H.-H. Fu, and R. Wu, *Phys. Rev. B* **102**, 035431 (2020).
- [26] R. Naaman, Y. Paltiel, and D. H. Waldeck, *Annu. Rev. Biophys.* **51**, 99 (2022).
- [27] R. Gutierrez, E. Díaz, R. Naaman, and G. Cuniberti, *Phys. Rev. B* **85**, 081404(R) (2012).
- [28] A.-M. Guo and Q.-F. Sun, *Phys. Rev. Lett.* **108**, 218102 (2012).
- [29] E. Medina, F. López, M. A. Ratner, and V. Mujica, *Europhys. Lett.* **99**, 17006 (2012).
- [30] Z.-G. Yu, *J. Phys. Chem. Lett.* **11**, 8638 (2020).
- [31] S.-Y. Xu, I. Belopolski, N. Alidoust, M. Neupane, G. Bian, C. Zhang, R. Sankar, G. Chang, Z. Yuan, C.-C. Lee *et al.*, *Science* **349**, 613 (2015).
- [32] G. Chang, B. J. Wieder, F. Schindler, D. S. Sanchez, I. Belopolski, S.-M. Huang, B. Singh, D. Wu, T.-R. Chang, T. Neupert *et al.*, *Nat. Mater.* **17**, 978 (2018).
- [33] D. S. Sanchez, I. Belopolski, T. A. Cochran, X. Xu, J.-X. Yin, G. Chang, W. Xie, K. Manna, V. Süß, C.-Y. Huang *et al.*, *Nature (London)* **567**, 500 (2019).
- [34] H. Li, S. Xu, Z.-C. Rao, L.-Q. Zhou, Z.-J. Wang, S.-M. Zhou, S.-J. Tian, S.-Y. Gao, J.-J. Li, Y.-B. Huang *et al.*, *Nat. Commun.* **10**, 5505 (2019).
- [35] M. A. Stolyarov, G. Liu, M. A. Bloodgood, E. Aytan, C. Jiang, R. Samnakay, T. T. Salguero, D. L. Nika, S. L. Rumyantsev, M. S. Shur *et al.*, *Nanoscale* **8**, 15774 (2016).
- [36] G. Liu, S. Rumyantsev, M. A. Bloodgood, T. T. Salguero, M. Shur, and A. A. Balandin, *Nano Lett.* **17**, 377 (2017).
- [37] Q. Zhang, C. Liu, X. Liu, J. Liu, Z. Cui, Y. Zhang, L. Yang, Y. Zhao, T. T. Xu, Y. Chen *et al.*, *ACS Nano* **12**, 2634 (2018).
- [38] Y. Zhu, D. A. Rehn, E. R. Antoniuk, G. Cheon, R. Freitas, A. Krishnapriyan, and E. J. Reed, *ACS Nano* **15**, 9851 (2021).
- [39] A. Kramer, M. L. Van de Put, C. L. Hinkle, and W. G. Vandenberghe, *npj 2D Mater. Appl.* **4**, 10 (2020).
- [40] F. Calavalle, M. Suárez-Rodríguez, B. Martín-García, A. Johansson, D. C. Vaz, H. Yang, I. V. Maznichenko, S. Ostanin, A. Mateo-Alonso, A. Chuvilin *et al.*, *Nat. Mater.* **21**, 526 (2022).
- [41] K. Shiota, A. Inui, Y. Hosaka, R. Amano, Y. Ōnuki, M. Hedo, T. Nakama, D. Hirobe, J.-I. Ohe, J.-I. Kishine, H. M. Yamamoto, H. Shishido, and Y. Togawa, *Phys. Rev. Lett.* **127**, 126602 (2021).
- [42] A. Inui, R. Aoki, Y. Nishiue, K. Shiota, Y. Kousaka, H. Shishido, D. Hirobe, M. Suda, J.-I. Ohe, J.-I. Kishine, H. M. Yamamoto, and Y. Togawa, *Phys. Rev. Lett.* **124**, 166602 (2020).

- [43] Y. Nabei, D. Hirobe, Y. Shimamoto, K. Shiota, A. Inui, Y. Kousaka, Y. Togawa, and H. M. Yamamoto, *Appl. Phys. Lett.* **117**, 052408 (2020).
- [44] A. Roy, F. T. Cerasoli, A. Jayaraj, K. Tenzin, M. B. Nardelli, and J. Sławińska, *npj Comput. Mater.* **8**, 243 (2022).
- [45] G. Sawitzki, D. Müller, and H. Hahn, *Mater. Res. Bull.* **15**, 753 (1980).
- [46] S. Jiang, H. Yin, G.-P. Zheng, B. Wang, S. Guan, and B.-J. Yao, *Phys. Chem. Chem. Phys.* **22**, 27441 (2020).
- [47] K. H. Choi, S. Cho, B. J. Jeong, B. Lee, J. Jeon, J. Kang, X. Zhang, H.-S. Oh, J.-H. Lee, H. K. Yu *et al.*, *J. Alloys Compd.* **927**, 166995 (2022).
- [48] M. A. U. Absor and F. Ishii, *Phys. Rev. B* **103**, 045119 (2021).
- [49] J. Sinova, S. O. Valenzuela, J. Wunderlich, C. H. Back, and T. Jungwirth, *Rev. Mod. Phys.* **87**, 1213 (2015).
- [50] V. M. Edelstein, *Solid State Commun.* **73**, 233 (1990).
- [51] A. Johansson, J. Henk, and I. Mertig, *Phys. Rev. B* **93**, 195440 (2016).
- [52] H. Jafari, A. Roy, and J. Sławińska, *Phys. Rev. Mater.* **6**, L091404 (2022).
- [53] I. Mertig, *Rep. Prog. Phys.* **62**, 237 (1999).
- [54] See Supplemental Material at <http://link.aps.org/supplemental/10.1103/PhysRevB.110.045434>, for more details which includes Refs. [42,58–68].
- [55] K. Wittel and R. Manne, *Theor. Chim. Acta* **33**, 347 (1974).
- [56] X. Zhang, J. Liu, and F. Liu, *Nano Lett.* **22**, 9000 (2022).
- [57] V. Kiran, S. P. Mathew, S. R. Cohen, I. Hernández Delgado, J. Lacour, and R. Naaman, *Adv. Mater.* **28**, 1957 (2016).
- [58] P. E. Blöchl, *Phys. Rev. B* **50**, 17953 (1994).
- [59] G. Kresse and D. Joubert, *Phys. Rev. B* **59**, 1758 (1999).
- [60] J. P. Perdew, K. Burke, and M. Ernzerhof, *Phys. Rev. Lett.* **77**, 3865 (1996).
- [61] G. Kresse and J. Furthmüller, *Phys. Rev. B* **54**, 11169 (1996).
- [62] M. Methfessel and A. T. Paxton, *Phys. Rev. B* **40**, 3616 (1989).
- [63] S. Grimme, J. Antony, S. Ehrlich, and H. Krieg, *J. Chem. Phys.* **132**, 154104 (2010).
- [64] S. O. Valenzuela and M. Tinkham, *Nature (London)* **442**, 176 (2006).
- [65] E. Saitoh, M. Ueda, H. Miyajima, and G. Tatara, *Appl. Phys. Lett.* **88**, 182509 (2006).
- [66] T. Kimura, Y. Otani, T. Sato, S. Takahashi, and S. Maekawa, *Phys. Rev. Lett.* **98**, 156601 (2007).
- [67] H. L. Wang, C. H. Du, Y. Pu, R. Adur, P. C. Hammel, and F. Y. Yang, *Phys. Rev. Lett.* **112**, 197201 (2014).
- [68] Y. Niimi and Y. Otani, *Rep. Prog. Phys.* **78**, 124501 (2015).